

Article

# Experimental Study of O<sub>2</sub>-Enriched CO<sub>2</sub> Production by BaCo<sub>0.8</sub>B<sub>0.2</sub>O<sub>3-δ</sub> (B=Ce, Al, Fe, Cu) Perovskites Sorbent for Marine Exhaust CO<sub>2</sub> Capture Application

Qiuwan Shen <sup>1</sup>, Zicheng Shao <sup>1</sup>, Shian Li <sup>1,\*</sup>, Guogang Yang <sup>1</sup>, Jinliang Yuan <sup>2</sup> and Xinxiang Pan <sup>1</sup>

<sup>1</sup> Marine Engineering College, Dalian Maritime University, Dalian 116000, China; shenqiuwan@dmlu.edu.cn (Q.S.); shaozicheng@dmlu.edu.cn (Z.S.); yanggg@dmlu.edu.cn (G.Y.); panxx@dmlu.edu.cn (X.P.)

<sup>2</sup> Faculty of Maritime and Transportation, Ningbo University, Ningbo 315211, China; yuanjinliang@nbu.edu.cn

\* Correspondence: lishian@dmlu.edu.cn

**Abstract:** An effective approach for reducing CO<sub>2</sub> emissions from marine exhaust is adopting oxyfuel combustion technology. A series of B-site doped BaCo<sub>0.8</sub>B<sub>0.2</sub>O<sub>3-δ</sub> (B=Ce, Al, Fe, Cu) perovskites as novel oxygen carrier applications were prepared by the sol-gel method. The oxygen desorption characteristics of the B-site doped BaCo<sub>0.8</sub>B<sub>0.2</sub>O<sub>3-δ</sub> perovskites and the effects of adsorption/desorption temperature, CO<sub>2</sub> volume flow rate, CO<sub>2</sub> partial pressures, and adsorption time were researched in the fixed bed reactor. The surface morphology and size of the oxygen carrier was observed by scanning electron microscope (SEM). Results showed that BaCo<sub>0.8</sub>Al<sub>0.2</sub>O<sub>3-δ</sub> and BaCo<sub>0.8</sub>Ce<sub>0.2</sub>O<sub>3-δ</sub> have comparable performance, considering the cost of the raw materials. BaCo<sub>0.8</sub>Al<sub>0.2</sub>O<sub>3-δ</sub> was selected as candidate for further study. The optimal adsorption/desorption temperature, CO<sub>2</sub> volume flow rate, CO<sub>2</sub> partial pressure and adsorption time for BaCo<sub>0.8</sub>Al<sub>0.2</sub>O<sub>3-δ</sub> were studied in detail. Results showed that the best operating parameters were determined to be 850 °C/850 °C for adsorption/desorption temperature, 200 mL/min for CO<sub>2</sub> volume flow rate, 100% CO<sub>2</sub> partial pressure, and 30 min for absorption time, respectively. Furthermore, multiple cycle results indicate that BaCo<sub>0.8</sub>Al<sub>0.2</sub>O<sub>3-δ</sub> sorbent has high reactivity and cyclic stability.

**Keywords:** marine exhaust; CO<sub>2</sub> capture; oxy-fuel combustion; perovskite



**Citation:** Shen, Q.; Shao, Z.; Li, S.; Yang, G.; Yuan, J.; Pan, X. Experimental Study of O<sub>2</sub>-Enriched CO<sub>2</sub> Production by BaCo<sub>0.8</sub>B<sub>0.2</sub>O<sub>3-δ</sub> (B=Ce, Al, Fe, Cu) Perovskites Sorbent for Marine Exhaust CO<sub>2</sub> Capture Application. *J. Mar. Sci. Eng.* **2021**, *9*, 661. <https://doi.org/10.3390/jmse9060661>

Academic Editor: Md Jahir Rizvi

Received: 1 June 2021

Accepted: 8 June 2021

Published: 15 June 2021

**Publisher's Note:** MDPI stays neutral with regard to jurisdictional claims in published maps and institutional affiliations.



**Copyright:** © 2021 by the authors. Licensee MDPI, Basel, Switzerland. This article is an open access article distributed under the terms and conditions of the Creative Commons Attribution (CC BY) license (<https://creativecommons.org/licenses/by/4.0/>).

## 1. Introduction

With the development of economic globalization, maritime transportation plays an important role in economic and social development [1]. The development of maritime transportation greatly increases the emission of carbon dioxide (CO<sub>2</sub>), which is a major greenhouse gas [2]. CO<sub>2</sub> emissions from maritime transportation represent around 3% of total annual anthropogenic greenhouse gas emissions [3]. The maritime sector is facing the serious challenge of significantly reducing its carbon emissions [4–6]. Global warming and climate change concerns have triggered global efforts to explore the carbon dioxide emissions reduction potentials and measures in the shipping industry. Alongside hull design, economy of scale, energy-saving devices, low carbon fuels and renewables, CO<sub>2</sub> capture and storage (CCS) technology, as a promising option to achieve significant reduction in CO<sub>2</sub> emissions, has received increasing attention over the past decade [7–9]. Despite developing other low-carbon shipping technologies, the application of CCS on board ships is considered an effective way to reduce CO<sub>2</sub> emissions.

CCS technology is currently mainly applied in power plants and industrial processes. As shown in Figure 1, there are three major approaches for CCS: post-combustion, pre-combustion and oxy-fuel combustion [10–12]. The pre-combustion method is to remove carbon before the fossil is burned. This method is technically difficult and expensive, and requires large equipment on the ship. The post-combustion capture method captures carbon

dioxide from the flue gas through chemical adsorption or liquefaction storage. However, the waste gas treatment device occupies a large space, affecting the cargo capacity of the ships. Furthermore, it is difficult and unsafe to store large amounts of carbon dioxide in the form of gas or liquid on ships. As such, oxy-fuel combustion is one promising technologies which has the potential to achieve a zero CO<sub>2</sub> emission [13–16]. In the oxy-fuel combustion technology, it is not air but pure oxygen that is used for the combustion of fossil fuels. Therefore, in theory, only water and carbon dioxide are produced after the combustion of fossil fuels, and high-purity carbon dioxide can be easily captured from the flue gas. Figure 2 shows a schematic diagram of an oxy-fuel combustion system. Moreover, oxy-fuel combustion technology is adequate for any existing or newly built ship type [3]. At present, there are few practical applications of oxy-fuel combustion technology on ships, and most of the related research is still at the basic research stage.

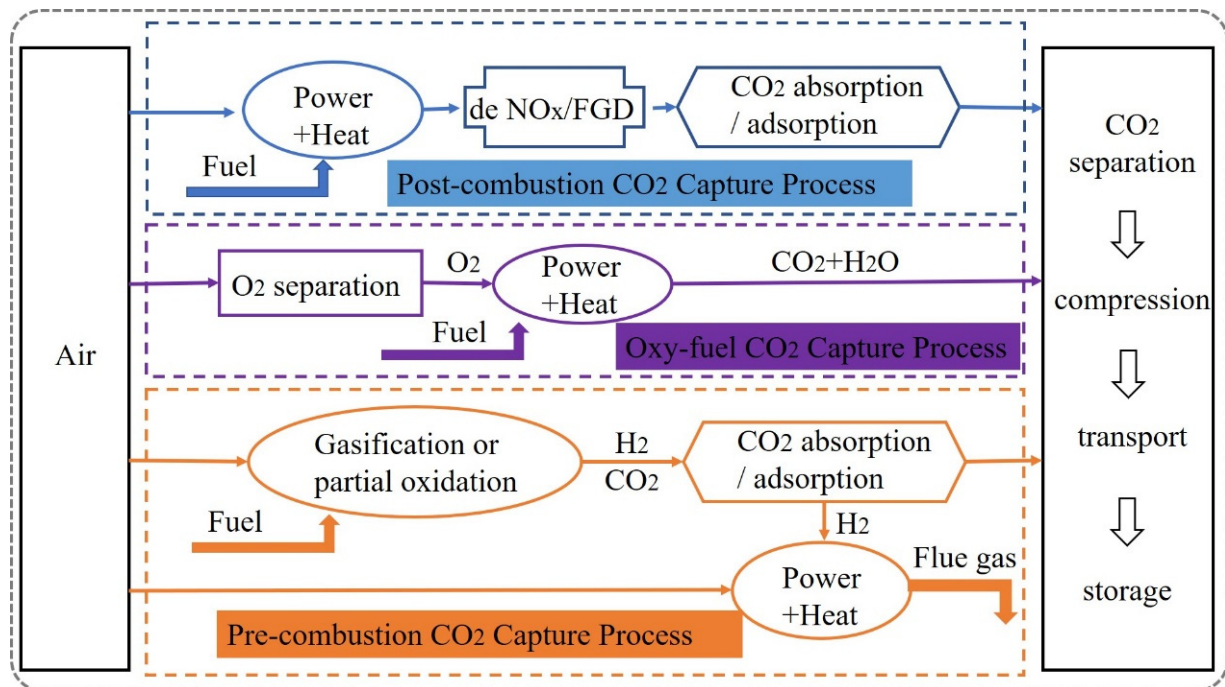


Figure 1. CO<sub>2</sub> capture and storage (CCS) technologies.

Oxy-fuel combustion has the following advantages: (1) up to 95% CO<sub>2</sub> concentration in the dry flue gas; (2) improved boiler efficiency; (3) reduced power consumption in flue gas treatment because of the small amount of flue gas involved; (4) reduced ship NO<sub>x</sub> and SO<sub>2</sub> emissions [17,18]. In oxy-fuel combustion, the energy-intensive air separation unit needs to provide a large amount of pure oxygen, which will increase costs [19]. For reducing the cost of oxygen production for oxy-fuel combustion, a new process for producing pure O<sub>2</sub> or O<sub>2</sub>/CO<sub>2</sub> gas streams by a perovskite-type oxygen carrier was proposed for oxy-fuel combustion technology [20]. Besides, replacing air with pure O<sub>2</sub> or O<sub>2</sub>/CO<sub>2</sub> gas streams for combustion will greatly reduce NO<sub>x</sub> and SO<sub>2</sub> emissions. Using two parallel fixed bed reactors with cobalt-based oxygen carriers, Zhang et al. continuously produced oxygen-rich CO<sub>2</sub> streams with oxygen concentrations in excess of 20% (21.7% by volume of oxygen in the air) [21].

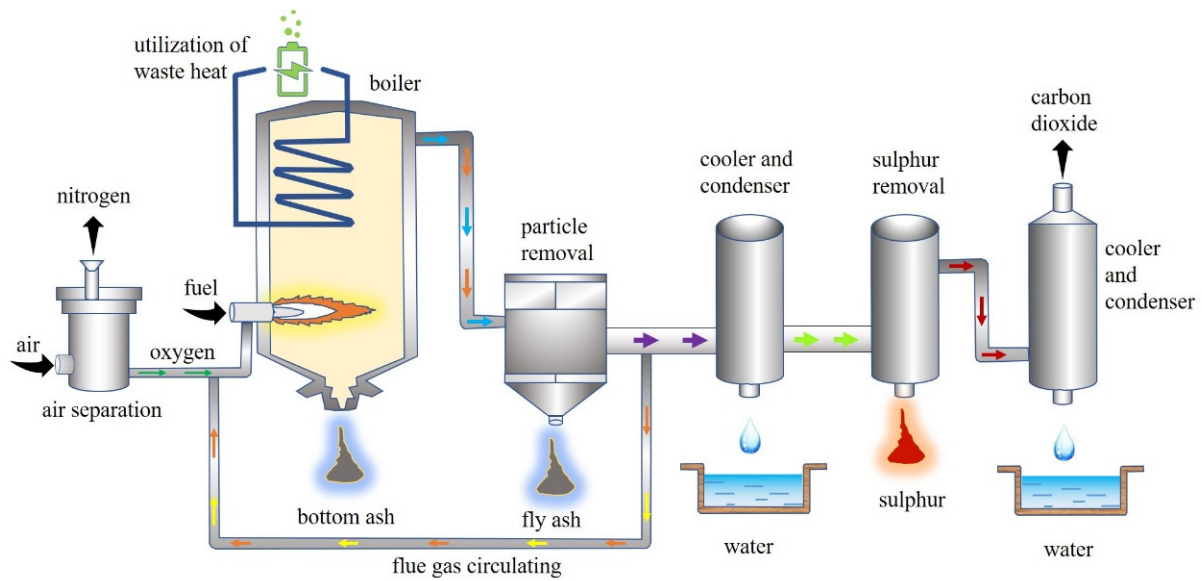


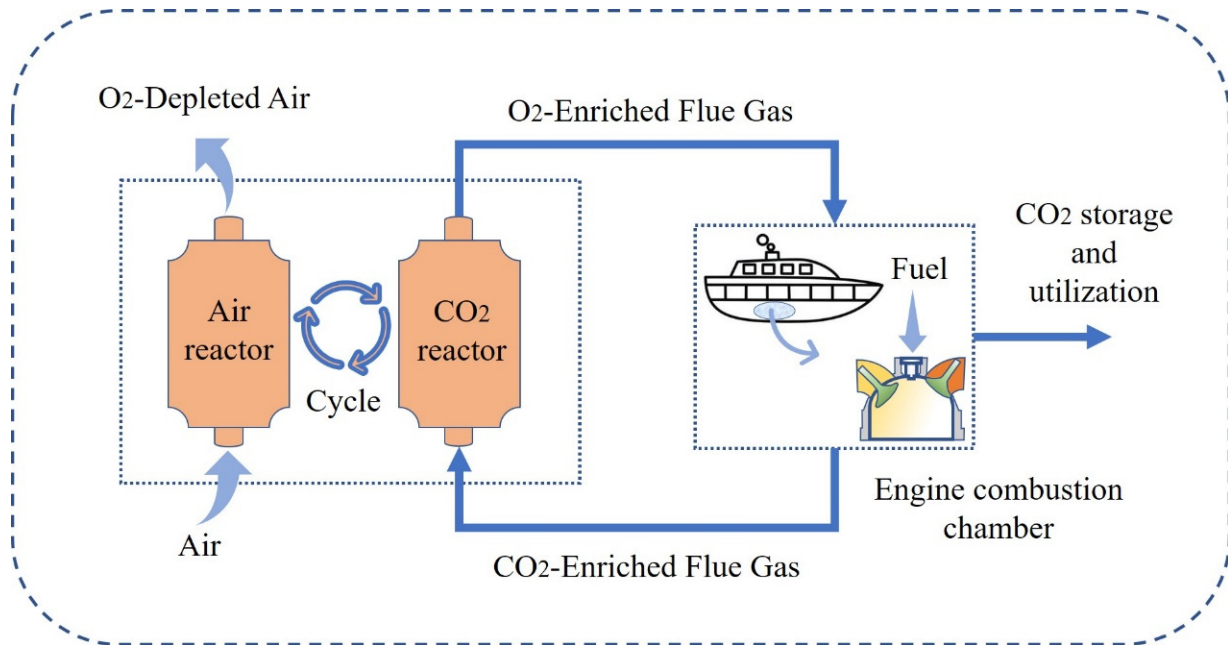
Figure 2. Schematic diagram of oxy-fuel combustion system.

Figure 3 shows the system of producing an oxygen-enriched CO<sub>2</sub> stream by a perovskite-type oxygen carrier for diesel engines: (1) In the adsorption process step, air is used as a feed gas to saturate the perovskite oxygen carrier with oxygen; (2) in the desorption process step, carbon dioxide is used as a sweep gas to desorb O<sub>2</sub> from the perovskite, producing an O<sub>2</sub>-enriched CO<sub>2</sub> flue gas stream; (3) the air is replaced by a stream of oxygen-enriched CO<sub>2</sub> which enters the combustion chamber of the engine to support combustion. There are some similar experimental studies. For example, Perez et al. carried out an experimental study on diesel combustion using simulated recirculated exhaust gas [22]. They found that the addition of CO<sub>2</sub> reduced the average combustion temperature, and oxygen-enriched conditions improved the combustion process of internal combustion engines under O<sub>2</sub>-enriched conditions. This cyclic process of oxygen adsorption and desorption is reversible. According to our previous study [23], a generalized description of the overall reaction stoichiometry in the reactor can be written as follows:



The general formula of perovskites is ABO<sub>3-δ</sub>, where A-cations are located on the edge of the crystal structure and play a major role in stabilization, and B-cations are located in the center of structure and mainly affect the catalytic activity because of their variable valence states [24–27]. Due to the excellent reactivity and oxygen mobility of perovskites, these compounds have attracted considerable attention [28]. Perovskite-type oxides ABO<sub>3</sub> can be customized to create various catalysts by changing the A- or the B-site metal ion. A series of fundamental studies on synergistic effects of A/B-site elements were studied from our group [16,17,29]. Zheng et al. found that SrCo<sub>1-x</sub>Fe<sub>x</sub>O<sub>3-δ</sub> has fine oxygen desorption performance [17]. Besides, in order to explore how dopant affects functional properties, they investigated the surface morphology, phase and crystal structure of SrCo<sub>1-x</sub>Fe<sub>x</sub>O<sub>3-δ</sub> through XRD, BET, etc. Our previous study found that BaCoO<sub>3-δ</sub> exhibited an excellent oxygen desorption performance. Shen et al. prepared perovskite materials of Ba–Sr–Co–Fe oxides by the microwave-assisted EDTA method (MWA-EDTA) [16]. They studied the effect of its surface morphology and element composition on oxygen desorption performance in detail through a variety of characterization methods. Yi et al. presented a systematic investigation on the influence of B-site cation composition on the performance of BaCo<sub>1-x-y</sub>Fe<sub>x</sub>Nb<sub>y</sub>O<sub>3-δ</sub> perovskite [29]. The results of these studies showed that Ba-Co-based perovskites have extraordinary ability to accommodate oxygen vacancies. Generally, the synthesis method has a greater impact on the properties of the material. Shen et al.

proposed a novelty process and an optimization study on the synthesis of the  $\text{BaCoO}_{3-\delta}$  perovskite powders using the microwave-assisted EDTA method. This study determined the optimal process parameters to prepare  $\text{BaCoO}_{3-\delta}$  perovskite by the microwave-assisted EDTA method [30].



**Figure 3.** Schematic diagram of producing oxygen-enriched CO<sub>2</sub> stream for marine diesel engines.

However, there is limited literature about B-site doping on Ba-Co-based perovskite as an oxygen carrier and applying it to oxy-fuel combustion technology. The development of a perovskite-type oxygen carrier with excellent oxygen adsorption/desorption performance and stable performance is the key to its actual production. In summary, Ba-Co-based perovskite  $\text{BaCo}_{0.8}\text{B}_{0.2}\text{O}_{3-\delta}$  (B=Ce, Al, Fe, Cu) doped with B-position cobalt base was selected as the candidate in this paper. The purpose of this paper is to develop Ba-Co-based perovskite powders with good oxygen-enriched CO<sub>2</sub> gas production performance as a potential oxygen carrier. In addition, optimal operating conditions of oxygen adsorption/desorption performance of Ba-Co-based perovskites were studied in detail through fixed bed experiments, which will provide a reference for a marine exhaust CO<sub>2</sub> capture application.

## 2. Material Preparation and Experiment

### 2.1. Oxygen Carrier Preparation Method

The perovskite powders were prepared using an ethylenediaminetetraacetic acid (EDTA)–citrate complex gel method [17]. The oxygen carriers in this study were prepared using nitrate forms such as Barium nitrate ( $\text{Ba}(\text{NO}_3)_2$ ), Cerium nitrate hexahydrate ( $\text{Ce}(\text{NO}_3)_3 \cdot 6\text{H}_2\text{O}$ ), Cobalt nitrate hexahydrate ( $\text{Co}(\text{NO}_3)_2 \cdot 6\text{H}_2\text{O}$ ), Aluminum nitrate nonahydrate ( $\text{Al}(\text{NO}_3)_3 \cdot 9\text{H}_2\text{O}$ ), Copper nitrate trihydrate ( $\text{Cu}(\text{NO}_3)_2 \cdot 3\text{H}_2\text{O}$ ), and iron nitrate nonahydrate ( $\text{Fe}(\text{NO}_3)_3 \cdot 9\text{H}_2\text{O}$ ) was used as a raw material to prepared the oxygen carrier. All the raw chemicals used were of analytical grade purity. Citric acid and ethylenediaminetetraacetic (EDTA) acid were used as complexing agents. The detailed EDTA–citrate complex gel method flow diagram is shown in Figure 4. For preparing  $\text{BaCo}_{0.8}\text{Al}_{0.2}\text{O}_{3-\delta}$  as an example, the detailed preparation procedures of the perovskite powders are as follows: (1) Dissolve barium nitrate, cobalt nitrate, and aluminum nitrate as reactants in deionized water, and the mole ratios of barium nitrate: cobalt nitrate: aluminum nitrate were controlled as 1:0.8:0.2; (2) dissolve citric acid and EDTA into a metal ion solution,

which serves as a precursor liquid. The mole ratios of total metal: citric acid: EDTA were controlled as 1:1.5:1; (3) the precursor liquid was stirred for 5 h at 80 °C in the water bath and dried 110 °C for 12 h after the gel appeared. After drying, it became a porous fluffy substance. (4) The porous fluffy substance was calcined in the air atmosphere at 450 °C for 30 min and then calcined in an air atmosphere of 850 °C for 8 h. (5) Finally, a dark powder was obtained after grinding and stored for characterization experiments in a clean test tube. The surface morphology of the synthesized samples was analyzed by scanning electron microscopy.

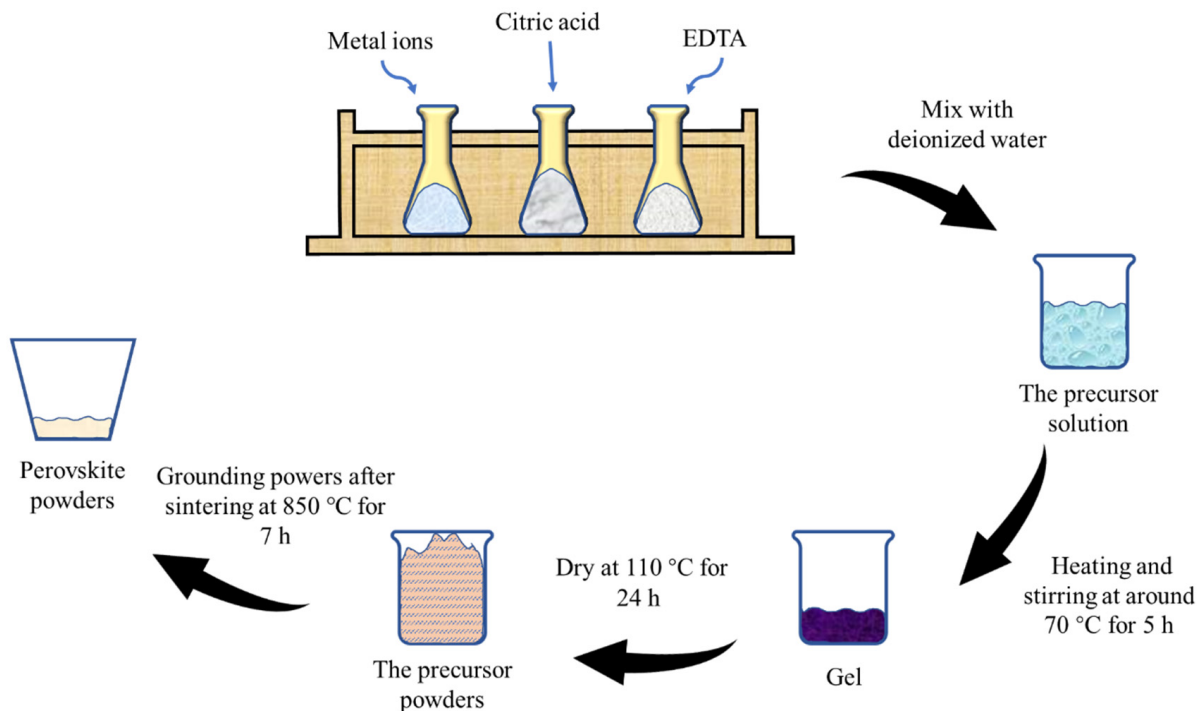


Figure 4. Flow chart of EDTA–citrate complex gel method.

### 2.2. Fixed Bed Reactor Experiment

In this paper, the experiments on the performance of oxygen carriers were all carried out in a fixed bed reactor system. The structure of this experimental system is shown in Figure 5. First, about 1.0 g of perovskite powders was packed in the middle of the quartz reactor with an inner diameter of 3 cm and a length of 80 cm. The reaction temperature is controlled by an external heating furnace. The whole process can be described as follows: during the O<sub>2</sub>-sorption process, air is used as the feed gas to saturate the sorbent with O<sub>2</sub>, while CO<sub>2</sub> is swept through the quartz glass reactor to desorb O<sub>2</sub> from the sorbent to obtain an O<sub>2</sub>-enriched CO<sub>2</sub> gas product. Meanwhile, the gas products enter the gas analyzer after being dried. Then the composition data of the gas products is recorded by a computerized data-acquisition system and used for subsequent analysis and research.

Here, the sample was heated to the designed temperature in 1 atm atmosphere. According to the data of the gas analyzer, the oxygen capacity was calculated using the following equation:

$$m_{O_2} = \frac{\sum P \times Q \times 10^{-3} \times M_{O_2}}{V_m \times 60} \quad (2)$$

where  $m_{O_2}$  (g) is the O<sub>2</sub> desorption amount for one gram of perovskite powder during the desorption,  $P$  (-) is the percentage of oxygen in gas products,  $Q$  (mL/min) is the gas volume flow,  $V_m$  (L/mol) is the gas molar volume and  $M_{O_2}$  (g/mol) is the molar mass of oxygen.

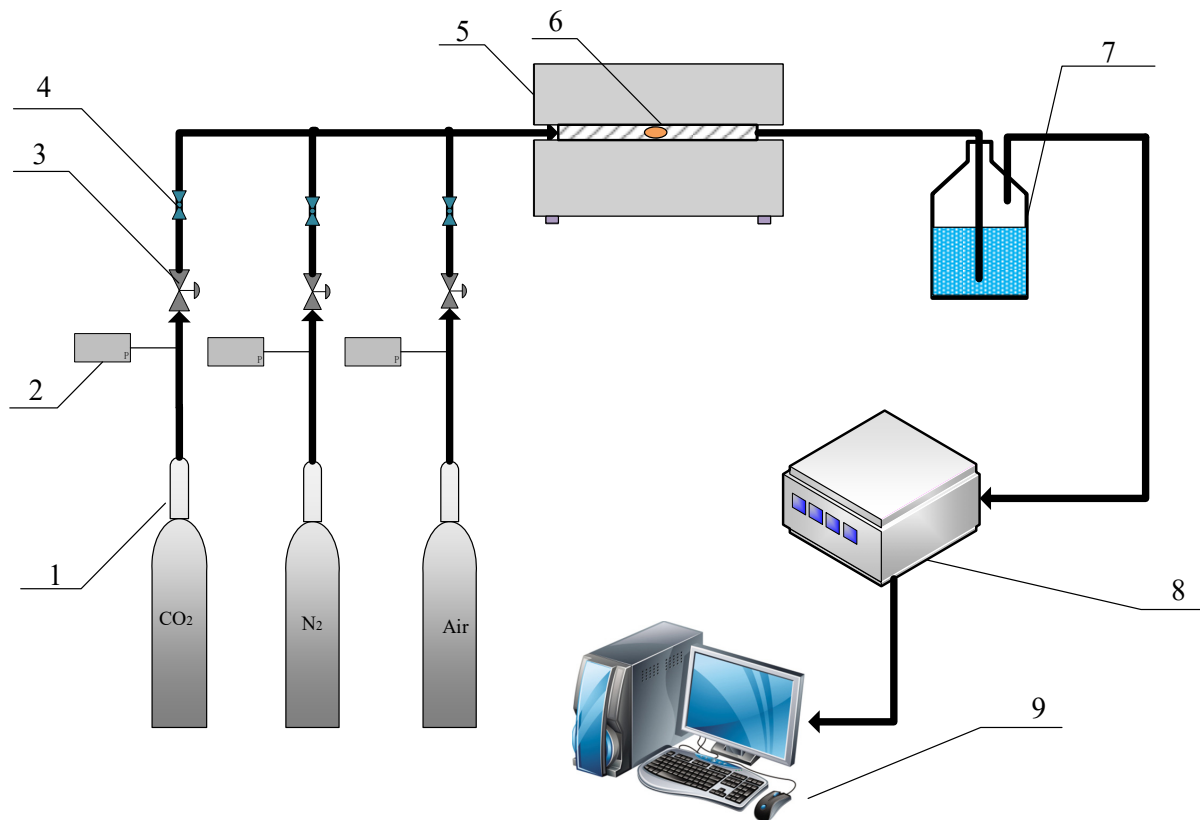


**Figure 5.** System diagram: (1) cylinder; (2) pressure gauge; (3) valve; (4) mass flow controller; (5) tube furnace; (6) quartz reactor; (7) adsorbent; (8) online gas analyzer; (9) computerized data-acquisition system.

### 2.3. Characterization

The crystalline structure of the samples was tested by X-ray diffraction (XRD, Rigaku, D/MAX-Ultima<sup>+</sup> diffractometer, Co K $\alpha$ ,  $\lambda = 1.7902 \text{ \AA}$ ). The diffractogram in the  $2\theta$  range of  $10\text{--}90^\circ$  was recorded with a scanning step of  $0.02^\circ$ . Its morphology was examined with scanning electron microscopy (SEM, SUPRA 55 SAPPHIRE, ZEISS, Germany). The atomic content was studied by energy-dispersive X-ray spectroscope (EDS) attached to the SEM instrument.

### 3. Results and Discussion

In this paper, four types of B-site doped cobalt-based perovskites were prepared using the sol-gel method:  $\text{BaCo}_{0.8}\text{Al}_{0.2}\text{O}_{3-\delta}$ ,  $\text{BaCo}_{0.8}\text{Cu}_{0.2}\text{O}_{3-\delta}$ ,  $\text{BaCo}_{0.8}\text{Fe}_{0.2}\text{O}_{3-\delta}$ , and  $\text{BaCo}_{0.8}\text{Ce}_{0.2}\text{O}_{3-\delta}$ , and the results of the fixed bed test are shown in Figure 6 (the adsorption/desorption temperatures are both  $850^\circ\text{C}$ , the gas volume flow rate is  $200 \text{ mL/min}$ , the partial pressure of  $\text{CO}_2$  is 100%, and the adsorption time is 30 min). As shown in Figure 6, the order of oxygen desorption amount was as follows:  $\text{BaCo}_{0.8}\text{Ce}_{0.2}\text{O}_{3-\delta} > \text{BaCo}_{0.8}\text{Al}_{0.2}\text{O}_{3-\delta} > \text{BaCo}_{0.8}\text{Fe}_{0.2}\text{O}_{3-\delta} > \text{BaCo}_{0.8}\text{Cu}_{0.2}\text{O}_{3-\delta}$ . The oxygen production amount of  $\text{BaCo}_{0.8}\text{Ce}_{0.2}\text{O}_{3-\delta}$  was the largest. This may be related to the large ion radius of Ce. B-site elements usually have a major influence on the properties of perovskite materials. Among Ce, Al, Fe, and Cu, the largest ionic radius of the B-site element was Ce ( $1.48 \text{ \AA}$ ). The bigger ionic radius of Ce resulted in the increase of lattice volume and led the contribution to oxygen ions transition in the crystal. The desorption process of  $\text{BaCo}_{0.8}\text{Ce}_{0.2}\text{O}_{3-\delta}$  and  $\text{BaCo}_{0.8}\text{Al}_{0.2}\text{O}_{3-\delta}$  was similar, and their reaction rates were faster. The oxygen production of  $\text{BaCo}_{0.8}\text{Ce}_{0.2}\text{O}_{3-\delta}$  was  $101.07 \text{ mg}$  and that of  $\text{BaCo}_{0.8}\text{Al}_{0.2}\text{O}_{3-\delta}$  was  $99.98 \text{ mg}$ , which are very close. Considering the lower cost of Al raw materials and faster response rate, here,  $\text{BaCo}_{0.8}\text{Al}_{0.2}\text{O}_{3-\delta}$  was selected as the candidate for further research. Besides, B-site substitution affects the surface adsorption activity, which also affects oxygen desorption

performance. Shen et al. found that substitution a Fe ion in  $\text{SrCo}_{0.8}\text{Fe}_{0.2}\text{O}_{3-\delta}$  with Cu reduced the oxygen desorption amount [23].

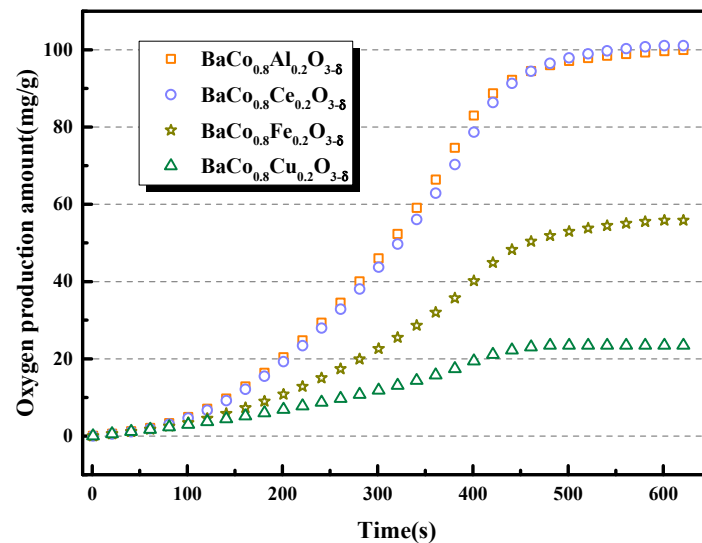
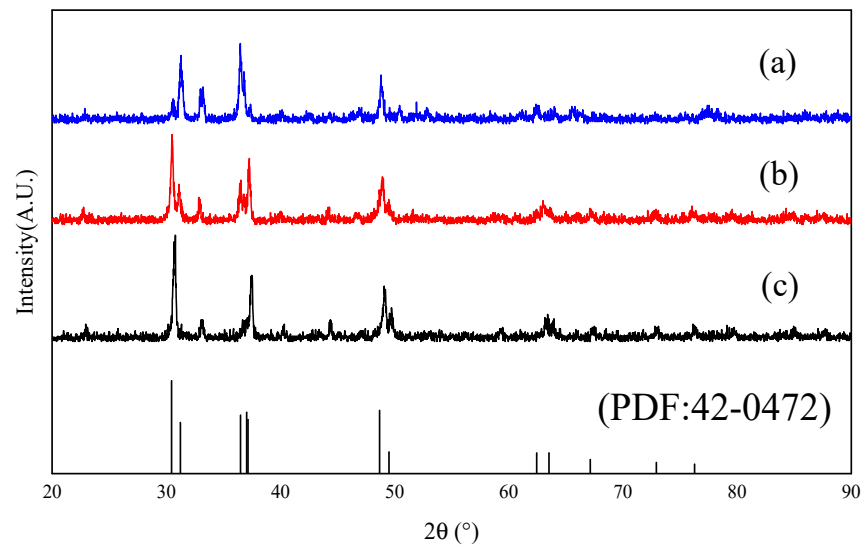


**Figure 6.** Oxygen desorption curves of  $\text{BaCo}_{0.8}\text{M}_{0.2}\text{O}_{3-\delta}$  ( $\text{M} = \text{Ce}, \text{Al}, \text{Fe}, \text{Cu}$ ) ( $\square$ :  $\text{BaCo}_{0.8}\text{Al}_{0.2}\text{O}_{3-\delta}$ ;  $\circ$ :  $\text{BaCo}_{0.8}\text{Ce}_{0.2}\text{O}_{3-\delta}$ ;  $\star$ :  $\text{BaCo}_{0.8}\text{Fe}_{0.2}\text{O}_{3-\delta}$ ;  $\triangle$ :  $\text{BaCo}_{0.8}\text{Cu}_{0.2}\text{O}_{3-\delta}$ ).

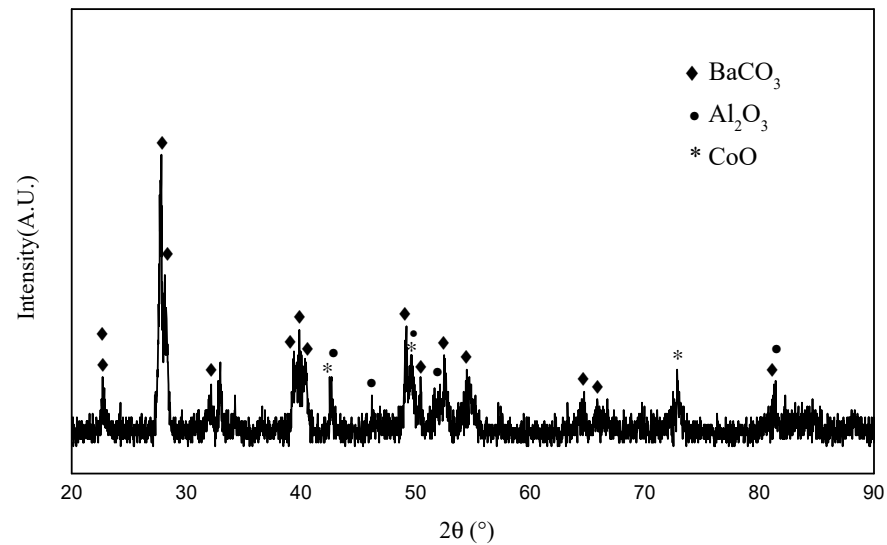
### 3.1. XRD and EDS Analysis

Figure 7 shows the XRD patterns of  $\text{BaCo}_{0.8}\text{Al}_{0.2}\text{O}_{3-\delta}$  powders. XRD characterization showed that the perovskite structure of the perovskite powder synthesized by the ethylenediaminetetraacetic acid (EDTA)–citrate complex gel method was indeed formed. As shown in Figure 7, the strong peaks occurred at  $30.5^\circ$ ,  $31.3^\circ$ ,  $36.5^\circ$ ,  $37.0^\circ$ ,  $37.2^\circ$ ,  $48.7^\circ$ ,  $49.5^\circ$ ,  $62.5^\circ$ ,  $63.5^\circ$ ,  $67.2^\circ$ ,  $73.0^\circ$ , and  $76.3^\circ$  corresponds to the crystal plane of (201), (121), (022), (220), (030), (231), (203), (420), (214), (340), (413), and (324) of  $\text{BaCoO}_{2.63}$  (JCPDS No.42-0472). With the increase of the number of oxygen desorption cycles, the diffraction peak of the sample almost did not change, which meant that the crystal structure of the synthesized sample was relatively stable. It can be seen from Figure 7 that the perovskite structure of the sample can still be maintained after one oxygen desorption process and 10 cycles of oxygen desorption, which also indicates that the  $\text{BaCo}_{0.8}\text{Al}_{0.2}\text{O}_{3-\delta}$  powders exhibits good cyclic stability. In addition, Figure 8 shows the XRD pattern of the solid products after the  $\text{BaCo}_{0.8}\text{Al}_{0.2}\text{O}_{3-\delta}$  carbonization reaction, and the main characteristic peaks of barium carbonate can be observed.

Through EDS analysis, it was confirmed that all elements in the catalyst were: Ba, Co, Al, and O. The selected area of SEM-EDS mapping is shown in Figure 9a, and the element distribution of the synthesized material is shown in Figure 9b–e. It can be seen that the main Ba, Co, Al, and O elements were consistent with the element composition of  $\text{BaCo}_{0.8}\text{Al}_{0.2}\text{O}_{3-\delta}$ . These elements were evenly distributed on the sample, and their distribution area corresponded to the shape of the sample in Figure 9a. The elemental composition of the synthesized catalyst was determined in Table 1 by SEM-EDS. It can be seen from Table 1 that the Ba/Co/Al ratio of the catalyst is close to 1:0.8:0.2 and the value is 1:0.8:0.26. According to the results of XRD and EDS, the  $\text{BaCo}_{0.8}\text{Al}_{0.2}\text{O}_{3-\delta}$  perovskite powder was successfully synthesized.



**Figure 7.** XRD patterns of  $\text{BaCo}_{0.8}\text{Al}_{0.2}\text{O}_{3-\delta}$  powders prepared by ethylenediaminetetraacetic acid (EDTA)–citrate complex gel method: (a) fresh sample; (b) reverted products after one cycles' oxygen desorption; (c) reverted products after 10 cycles' oxygen desorption.



**Figure 8.** XRD patterns of reaction products of the carbonation reaction of  $\text{BaCo}_{0.8}\text{Al}_{0.2}\text{O}_{3-\delta}$  powders.

### 3.2. Effect of the Adsorption Temperature on Oxygen Desorption Performance

In the following chapters, we studied the effect of operating parameters on the oxygen production performance of  $\text{BaCo}_{0.8}\text{Al}_{0.2}\text{O}_{3-\delta}$ .

According to the previous results of our group [16], the adsorption temperature and desorption temperature have the greatest impact on the performance of the oxygen carrier. Figure 10a shows the oxygen adsorption performance of  $\text{BaCo}_{0.8}\text{Al}_{0.2}\text{O}_{3-\delta}$  at different adsorption temperatures from 700 °C to 900 °C and Figure 10b shows the oxygen production amount of  $\text{BaCo}_{0.8}\text{Al}_{0.2}\text{O}_{3-\delta}$  at different adsorption temperatures of 700 °C, 800 °C, 850 °C and 900 °C, respectively (the desorption temperature is 850 °C, the partial pressure of  $\text{CO}_2$  is 100%, the adsorption time is 30 min, and the  $\text{CO}_2$  volume flow rate is  $200 \text{ mL}\cdot\text{min}^{-1}$ ).  $\text{BaCo}_{0.8}\text{Al}_{0.2}\text{O}_{3-\delta}$  showed no significant effect when the temperature was raised from 800 °C to 850 °C, but at 900 °C the lowest oxygen production of 85.5 mg was recorded.  $\text{BaCo}_{0.8}\text{Al}_{0.2}\text{O}_{3-\delta}$  had maximum oxygen production at 850 °C, but the oxygen production decreased as the temperature increased from 850 °C to 900 °C. This might be because the carbonation reaction between  $\text{CO}_2$  and perovskite needs a higher temperature,

but too high of a temperature will lead to perovskite sintering, which will affect the oxygen desorption performance. It is clear that 850 °C was the ideal adsorption temperature in this condition.

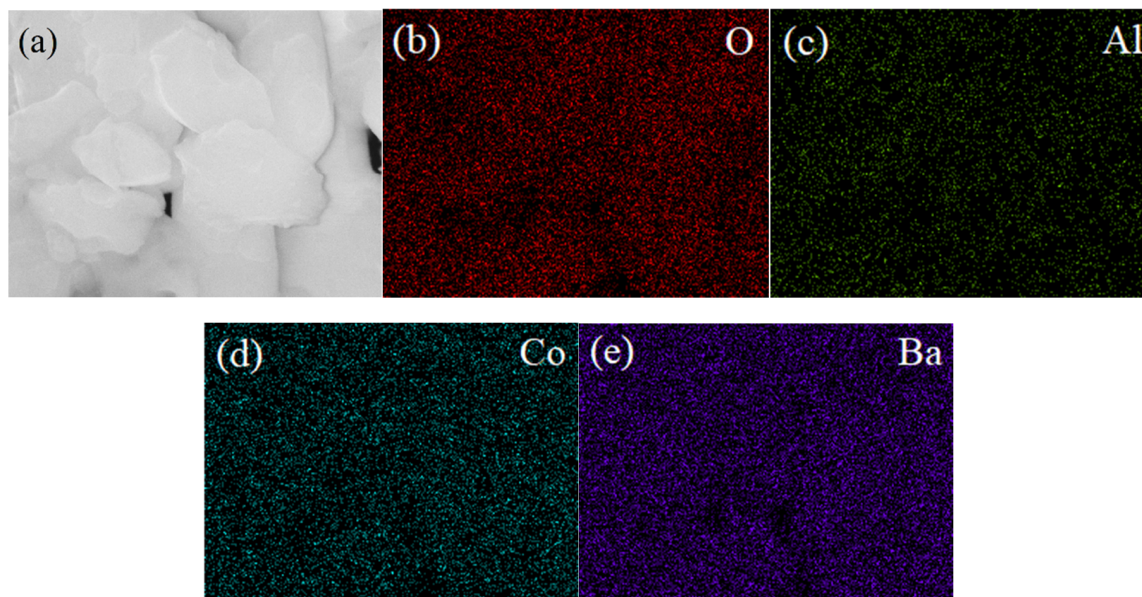


**Figure 9.** SEM-EDS mapping images of  $\text{BaCo}_{0.8}\text{Al}_{0.2}\text{O}_{3-\delta}$  powders: (a) the selected area of SEM-EDS mapping; (b) oxygen; (c) aluminium; (d) cobalt; (e) barium.

**Table 1.** Elemental composition of the as-synthesized catalysts.

Elements	Mass Percentage (%)	Atomic Percentage (%)
Ba	52.34	15.41
Co	17.97	12.33
Al	2.69	4.03
O	27.00	68.24

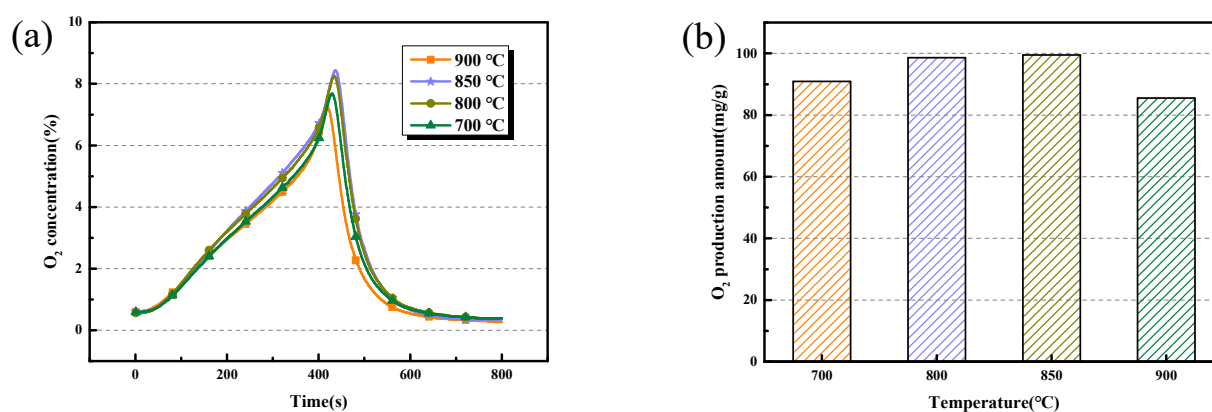


**Figure 10.** (a) Oxygen desorption curves of  $\text{BaCo}_{0.8}\text{Al}_{0.2}\text{O}_{3-\delta}$  at different adsorption temperatures. (b) Comparison of oxygen desorption amount for  $\text{BaCo}_{0.8}\text{Al}_{0.2}\text{O}_{3-\delta}$  at different adsorption temperatures.

### 3.3. Effect of the Desorption Temperature on Oxygen Desorption Performance

From Figure 11a, it can be observed that there are obvious differences in the desorption process at different desorption temperatures. The response at 850 °C is the fastest, the oxygen concentration that can be reached is the highest, and the desorption time is the longest. That is, the oxygen quality produced by  $\text{BaCo}_{0.8}\text{Al}_{0.2}\text{O}_{3-\delta}$  is the best when the

desorption temperature is 850 °C. The oxygen production amount of  $\text{BaCo}_{0.8}\text{Al}_{0.2}\text{O}_{3-\delta}$  at different desorption temperatures of 700 °C, 800 °C, 850 °C, and 900 °C is shown in Figure 11b.  $\text{BaCo}_{0.8}\text{Al}_{0.2}\text{O}_{3-\delta}$  showed a maximum oxygen production of 99.5 mg at 850 °C followed by 59.11 mg, 66.01 mg and 72.13 mg at 750 °C, 800 °C, and 900 °C, respectively (the adsorption temperature is 850 °C, the partial pressure of  $\text{CO}_2$  is 100%, the adsorption time is 30 min, and its  $\text{CO}_2$  volume flow rate is  $200 \text{ mL}\cdot\text{min}^{-1}$ ). As shown in Figure 11b, the oxygen production at 850 °C is nearly double that at 750 °C, 800 °C, and 900 °C. The low temperature effect is not good because a low temperature cannot provide enough activation energy and too high of a temperature will cause sintering, which will result in the degradation of oxygen carrier performance.

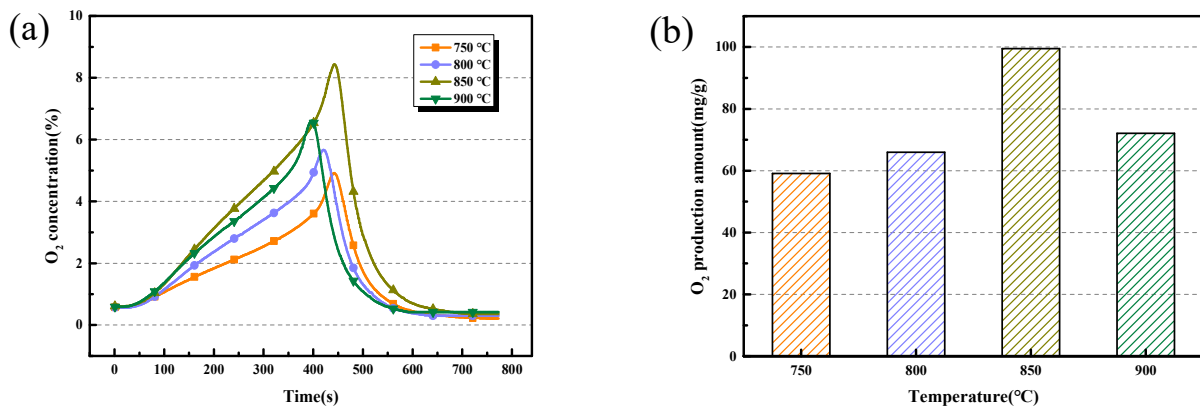


**Figure 11.** (a) Oxygen desorption curves of  $\text{BaCo}_{0.8}\text{Al}_{0.2}\text{O}_{3-\delta}$  at different desorption temperatures. (b) Comparison of oxygen desorption amount for  $\text{BaCo}_{0.8}\text{Al}_{0.2}\text{O}_{3-\delta}$  at different desorption temperatures.

### 3.4. Effect of the $\text{CO}_2$ Volume Flow Rates on Oxygen Desorption Performance

For the  $\text{CO}_2$  volume flow rates experiments, the optimal conditions that were found remain unchanged (the adsorption/desorption temperature are both 850 °C, the adsorption time is 30 min, and the partial pressure is 100%). Figure 12a shows the desorption performance of  $\text{BaCo}_{0.8}\text{Al}_{0.2}\text{O}_{3-\delta}$  is significantly different in the  $\text{CO}_2$  inlet volume flow rates range of 50–300 mL/min. The experimental results show that the volume flow rate of carbon dioxide has a significant effect on the reaction rate of the oxygen carrier desorption process. As the carbon dioxide purge rate increases, the response speed of the oxygen desorption process also increases significantly. This may be due to the fact that carbon dioxide can contact more perovskite surface area in a short time when the carbon dioxide purging speed increases. The oxygen production amount of  $\text{BaCo}_{0.8}\text{Al}_{0.2}\text{O}_{3-\delta}$  at different  $\text{CO}_2$  volumetric flow rates is shown in Figure 12b. Figure 12b shows that the oxygen production amount of  $\text{BaCo}_{0.8}\text{Al}_{0.2}\text{O}_{3-\delta}$  is the highest when the volume flow rate is 50 mL/min, but the desorption process is as long as 40 min. This is not a good choice for industrial applications. The oxygen production amount of  $\text{BaCo}_{0.8}\text{Al}_{0.2}\text{O}_{3-\delta}$  is the lowest when the  $\text{CO}_2$  volume flow rate is 300 mL/min. Compared with 100 mL/min, the 200 mL/min desorption process takes less time, only about 10 min, and the oxygen production is 6.7% more. This result is obvious that the comprehensive performance of oxygen desorption is the best when the purge rate is 200 mL/min.

### 3.5. Effect of the $\text{CO}_2$ Partial Pressures on Oxygen Desorption Performance

Here, the  $\text{CO}_2$  partial pressures will affect the performance of the oxygen carrier. The effect of  $\text{CO}_2$  partial pressures (the  $\text{CO}_2$  partial pressures is 20%, 50%, 80%, 100%) on the reduction reaction of  $\text{BaCo}_{0.8}\text{Al}_{0.2}\text{O}_{3-\delta}$  was investigated in fixed bed (the adsorption/desorption temperatures are both 850 °C, the adsorption time is 30 min, and its  $\text{CO}_2$  volume flow rate is  $200 \text{ mL}\cdot\text{min}^{-1}$ ). The partial pressure of carbon dioxide has an important influence on the carbonation reaction of perovskite and  $\text{CO}_2$ . The performance of  $\text{BaCo}_{0.8}\text{Al}_{0.2}\text{O}_{3-\delta}$  with time of desorption process can be seen in Figure 13a. Figure 13b

shows the O<sub>2</sub> production amount of BaCo<sub>0.8</sub>Al<sub>0.2</sub>O<sub>3-δ</sub> at different CO<sub>2</sub> partial pressures of 20%, 50%, 80% and 100%, respectively. It indicates that the O<sub>2</sub> production amount decreases as the CO<sub>2</sub> partial pressures become higher, and the oxygen concentration can be maintained at a higher level for a longer time during the entire desorption process. Therefore, the higher the partial pressure of carbon dioxide, the better the quality of the O<sub>2</sub>-enriched stream produced. As the number of cycles increases, the partial pressure of CO<sub>2</sub> in the flue gas will increase when real flue gas is used as purge gas during the oxygen desorption process.

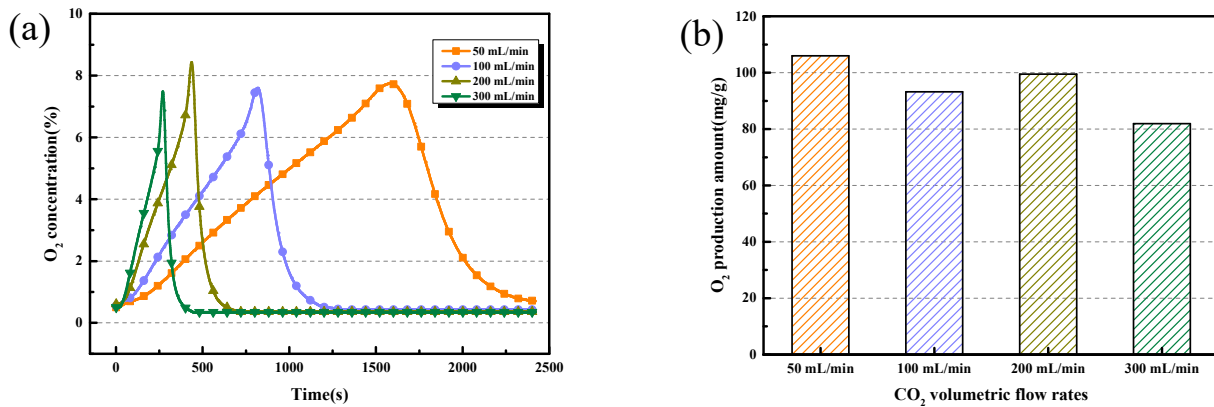


**Figure 12.** (a) Oxygen desorption curves of BaCo<sub>0.8</sub>Al<sub>0.2</sub>O<sub>3-δ</sub> at different CO<sub>2</sub> volume flow rates. (b) Comparison of oxygen desorption amount for BaCo<sub>0.8</sub>Al<sub>0.2</sub>O<sub>3-δ</sub> at different CO<sub>2</sub> volume flow rates.

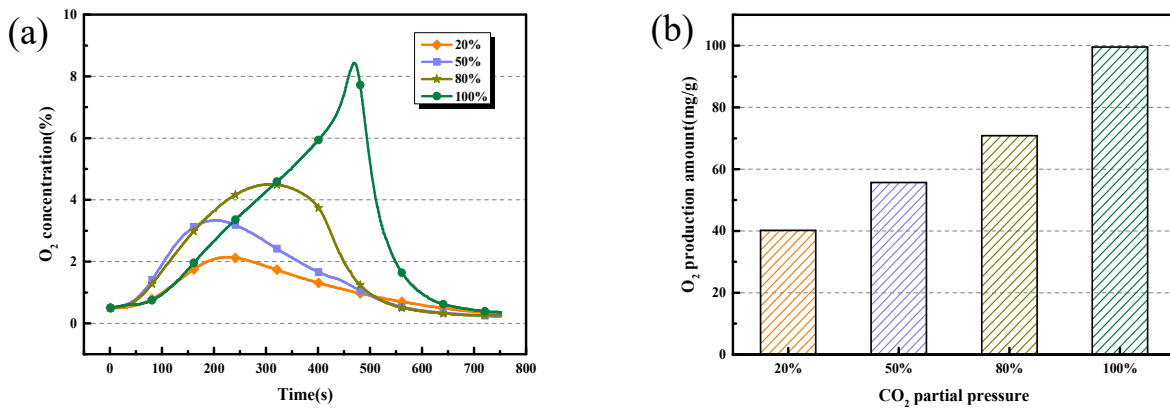


**Figure 13.** (a) Oxygen desorption curves of BaCo<sub>0.8</sub>Al<sub>0.2</sub>O<sub>3-δ</sub> at different CO<sub>2</sub> partial pressures. (b) Comparison of oxygen desorption amount for BaCo<sub>0.8</sub>Al<sub>0.2</sub>O<sub>3-δ</sub> at different CO<sub>2</sub> partial pressures.

### 3.6. Effect of the Adsorption Time on Oxygen Desorption Performance

The oxygen adsorption time has a great influence on actual production activities. The shorter the adsorption time, the less fixed bed equipment is needed to provide the required concentration. Therefore, it is necessary to determine the optimal oxygen adsorption time. Take the oxygen adsorption time (10 min, 20 min, 30 min, 40 min) as the experimental variable and do four fixed bed tests, respectively (the adsorption/desorption temperatures are both 850 °C, CO<sub>2</sub> volume flow rate is 200 mL·min<sup>-1</sup>, and partial pressure is 100%). From Figure 14, it can be seen that the response speed and time of O<sub>2</sub> desorption process does not show an apparent decrease with an increasing of time. When the adsorption time is too long, the porosity of the material will decrease, thus affecting the oxygen desorption performance [30]. As shown in Figure 14, the O<sub>2</sub> adsorption in CO<sub>2</sub> atmosphere was quantified as mass variation. It can be observed that 30 min is the best choice for laboratory tests because the time is shorter and the O<sub>2</sub> desorption performance is the best; however,

in real production activities, this paper argues that 10 min should be selected as the actual adsorption time because it only takes a third of the time and the oxygen production amount is only reduced by 6% compared to the adsorption time of 30 min.

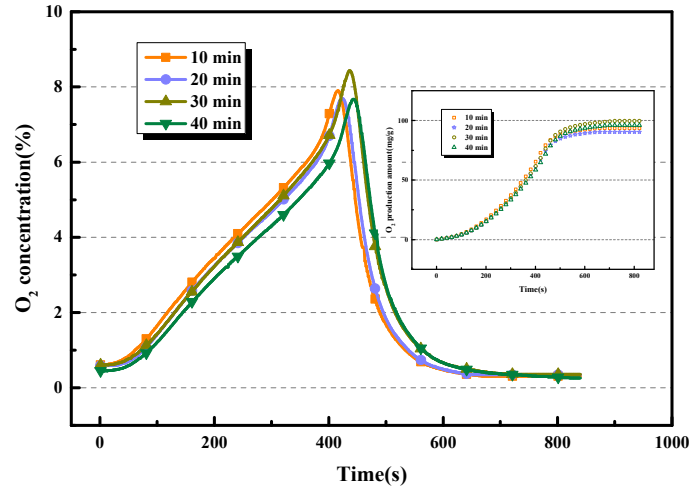


Figure 14. Oxygen desorption curves of  $BaCo_{0.8}Al_{0.2}O_{3-\delta}$  at different adsorption times.

### 3.7. Cycle Behavior of the Oxygen Carrier

Since the oxygen carrier is used repeatedly in actual production activities, the cycle adsorption/desorption performance of the oxygen carrier is especially important in practical applications. Through the above experiments, the optimal adsorption/desorption temperature,  $CO_2$  purge rate,  $CO_2$  partial pressure, and adsorption time of the  $BaCo_{0.8}Al_{0.2}O_{3-\delta}$  oxygen carrier were determined for the fixed bed experiments. The stability experiment of the adsorption/desorption behavior of the oxygen carrier was carried out. Figures 15 and 16 show that the oxygen desorption process for each cycle is essentially the same. As shown in Figure 15, it can be seen that oxygen production amount declines a little with the time of cycle. It decreased by 14.5% after 5 cycles and decreased by 18.6% after 10 cycles. The reason is because the oxygen carrier is sintered after multiple cycles and the impurities on the surface increase, which reduces the specific surface area of the oxygen carrier and the number of oxygen vacancies. Obviously, the  $BaCo_{0.8}Al_{0.2}O_{3-\delta}$  oxygen carrier exhibits the good cyclic reactivity and stability and can enable it to provide stable  $O_2/CO_2$  cyclic steam for oxy-fuel combustion.

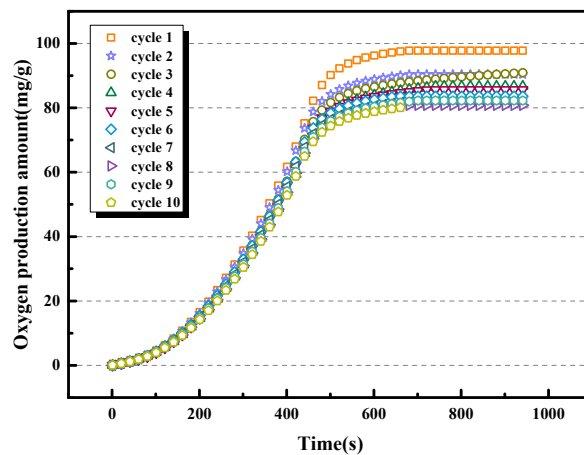


Figure 15. Cycle oxygen desorption curves of  $BaCo_{0.8}Al_{0.2}O_{3-\delta}$ .

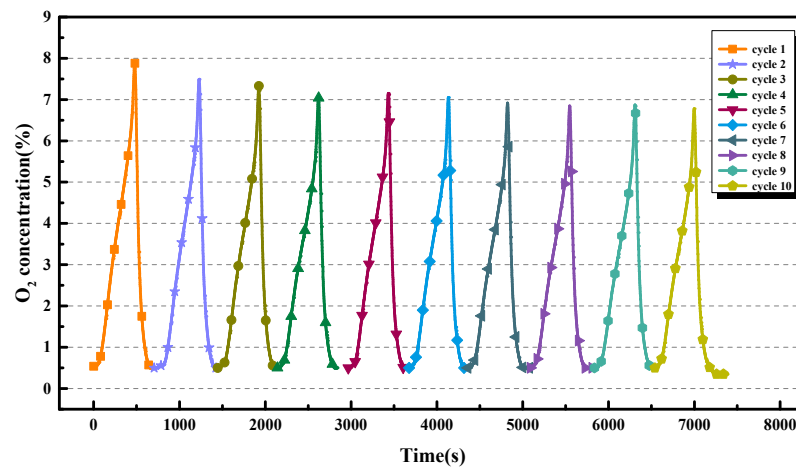


Figure 16. Cyclic capability of BaCo<sub>0.8</sub>Al<sub>0.2</sub>O<sub>3-δ</sub>.

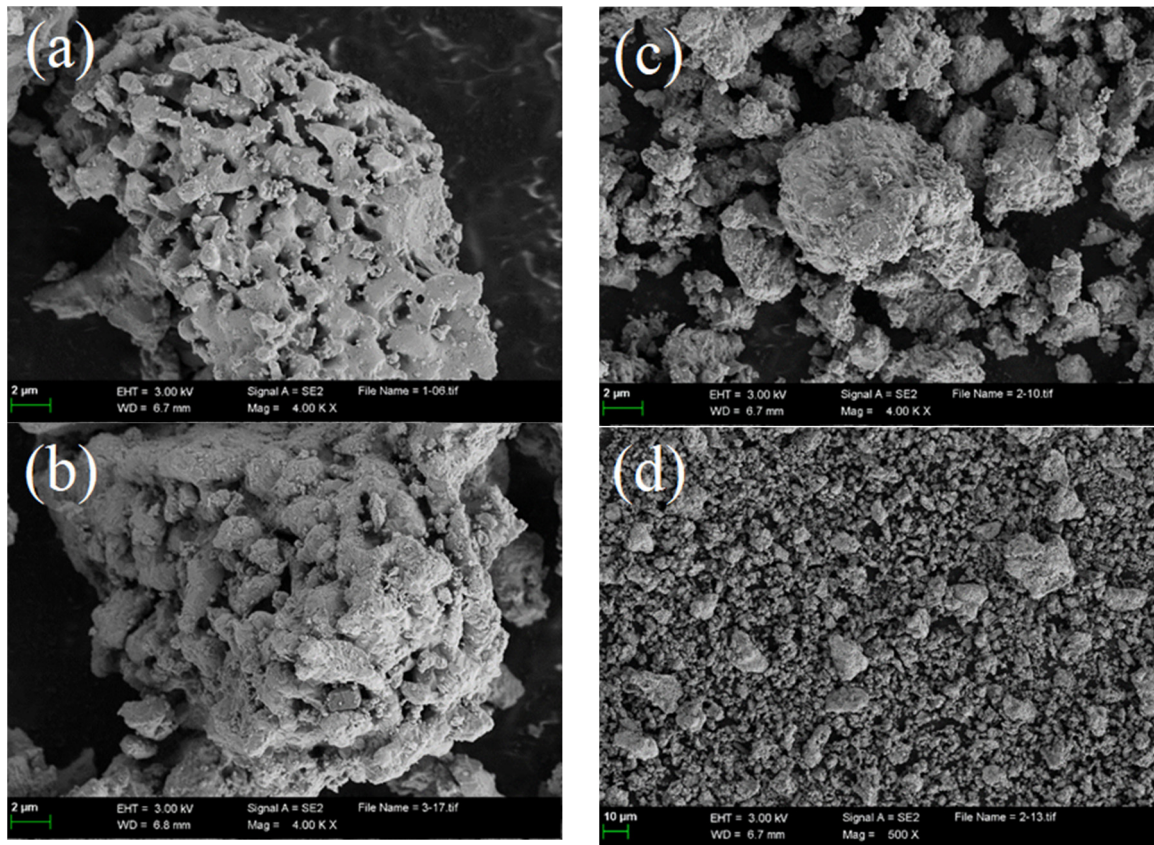
Currently, the most efficient diesel engine still wastes about 50% of its energy. This energy is lost to the atmosphere in the form of waste heat along with the exhaust gas. As shown in Table 2 below, the temperature range of ship engine waste heat can match the operating temperature of the perovskite adsorbent [31], which provides potential for the marine application of this technology.

Table 2. Temperature range of main waste heat sources.

Waste Heat Source	Temperature Range
Waste incinerator	850–1200 °C
Engine exhaust gas	200–500 °C
Scavenge air (compressor outlet)	100–160 °C
Engine cooling water	70–125 °C

### 3.8. SEM Characteristics

Observe the surface morphology and size of the oxygen carrier before and after adsorbing oxygen by scanning electron microscope (SEM). As shown in Figure 17a at a magnification of 4000, the fresh sample has a porous structure, and it can be observed that a lot of pores around 0.3–1.5 μm in size are distributed inside the sample particles. The porous surface of this structure contributes to the rapid chemical reaction rate during carbonation [17]. Figure 17b shows the sample after desorption. The pores on the surface of the particles become smaller or disappear, the particles become fuller, and the surface is covered with impurities. The fixed bed cyclic test shows that the oxygen production amount of the second cycle is 7.5% lower than that of the first cycle, indicating that the disappearance of micropores and the coverage of impurities lead to a decrease in oxygen release performance. Figure 17c shows the sample after the fixed bed cycle test. Compared with Figure 17a, the small pores inside the particles are reduced and the covered impurities are further increased. This corroborates the results shown in Figure 15. As seen in Figure 17d, a uniform size is not obtained after grinding at magnification of 500, and the particle size distribution is in the range of 4–45 μm.



**Figure 17.** SEM images of BaCo<sub>0.8</sub>Al<sub>0.2</sub>O<sub>3-δ</sub> in various states: (a) Fresh (4000×); (b) used but no oxygen absorbed (4000×); (c) adsorbing oxygen after adsorption and desorption cycles (4000×); (d) adsorbing oxygen after adsorption and desorption cycles (500×).

#### 4. Conclusions

BaCo<sub>0.8</sub>B<sub>0.2</sub>O<sub>3-δ</sub> (B=Ce, Al, Fe, Cu) perovskites were prepared by the EDTA–citrate complex gel method and used to produce O<sub>2</sub>–CO<sub>2</sub> gas mixture at a high temperature for CO<sub>2</sub> capture from marine diesel engines. The optimum reaction conditions of BaCo<sub>0.8</sub>Al<sub>0.2</sub>O<sub>3-δ</sub> perovskite powders were studied by fixed bed experiments.

The results show that the order of oxygen desorption amount was as follows: BaCo<sub>0.8</sub>Ce<sub>0.2</sub>O<sub>3-δ</sub> > BaCo<sub>0.8</sub>Al<sub>0.2</sub>O<sub>3-δ</sub> > BaCo<sub>0.8</sub>Fe<sub>0.2</sub>O<sub>3-δ</sub> > BaCo<sub>0.8</sub>Cu<sub>0.2</sub>O<sub>3-δ</sub>. The oxygen production amount of 1g BaCo<sub>0.8</sub>Al<sub>0.2</sub>O<sub>3-δ</sub> perovskite powders can reach 99.5 mg after one adsorption and desorption cycle. SEM results show that the fresh samples of BaCo<sub>0.8</sub>Al<sub>0.2</sub>O<sub>3-δ</sub> had a porous structure, and the particles were covered by impurities after the cycle due to sintering and other reasons. In addition, the experimental results showed that the best operating parameters were determined to be 850 °C/850 °C for adsorption/desorption temperature, 200 mL/min for CO<sub>2</sub> volume flow rate, 100% CO<sub>2</sub> partial pressure, and 30 min for absorption time, respectively. Furthermore, BaCo<sub>0.8</sub>Al<sub>0.2</sub>O<sub>3-δ</sub> exhibits good cyclic reactivity and stability and can provide stable O<sub>2</sub>/CO<sub>2</sub> mixed gas for oxy-fuel combustion. However, more cyclic tests are needed to assess the practical CO<sub>2</sub> capture application of marine exhaust.

**Author Contributions:** Conceptualization, Q.S.; investigation, S.L.; resources, S.L.; data curation, Z.S.; figures and tables: S.L.; writing—original draft preparation, Q.S., Z.S.; writing—review and editing, S.L., Z.S., G.Y., J.Y., X.P.; supervision, Q.S.; funding acquisition, Q.S., S.L., G.Y. All authors have read and agreed to the published version of the manuscript.

**Funding:** This research was funded by THE NATIONAL NATURAL SCIENCE FOUNDATION OF CHINA OF FUNDER, grant number 52001045, CHINA POSTDOCTORAL SCIENCE FOUNDATION OF FUNDER, grant number 2019M651097 and 2019M651094, NATURAL SCIENCE FOUNDATION

OF LIAONING PROVINCE OF FUNDER, grant number 2019-ZD-0154 and 2020-HYLH-38, and DA-LIAN CITY INNOVATIVE SUPPORT PROGRAM FOR HIGH-LEVEL TALENTS OF FUNDER, grant number 2019RQ036." and "The APC was funded by THE NATIONAL NATURAL SCIENCE FOUNDATION OF CHINA OF FUNDER, grant number 52001045.

**Institutional Review Board Statement:** Not applicable.

**Informed Consent Statement:** Not applicable.

**Data Availability Statement:** Not applicable.

**Acknowledgments:** This work was supported by the National Natural Science Foundation of China (No. 52001045), China Postdoctoral Science Foundation (No.2019M651097 and No.2019M651094), Natural Science Foundation of Liaoning Province (No.2019-BS-026, No.2019-ZD-0154 and No. 2020-HYLH-38), Dalian City Innovative Support Program for High-Level Talents (No. 2019RQ036) and the Fundamental Research Funds for the Central Universities of China of Funder (3132019327).

**Conflicts of Interest:** The authors declare no conflict of interest.

## References

- Xing, H.; Spence, S.; Chen, H. A comprehensive review on countermeasures for CO<sub>2</sub> emissions from ships. *Renew. Sustain. Energy Rev.* **2020**, *134*, 110222. [\[CrossRef\]](#)
- Sui, C.; Stapersma, D.; Visser, K.; de Vos, P.; Ding, Y. Energy effectiveness of ocean-going cargo ship under various operating conditions. *Ocean Eng.* **2019**, *190*, 106473. [\[CrossRef\]](#)
- Bouman, E.A.; Lindstad, E.; Riialand, A.I.; Strømman, A.H. State-of-the-art technologies, measures, and potential for reducing GHG emissions from shipping—A review. *Transp. Res. Part D Transp. Environ.* **2017**, *52*, 408–421. [\[CrossRef\]](#)
- Van, T.C.; Ramirez, J.; Rainey, T.; Ristovski, Z.; Brown, R.J. Global impacts of recent IMO regulations on marine fuel oil refining processes and ship emissions. *Transp. Res. Part D Transp. Environ.* **2019**, *70*, 123–134. [\[CrossRef\]](#)
- Johansson, L.; Jalkanen, J.P.; Kukkonen, J. Global assessment of shipping emissions in 2015 on a high spatial and temporal resolution. *Atmos. Environ.* **2017**, *167*, 403–415. [\[CrossRef\]](#)
- Rehmatulla, N.; Calleya, J.; Smith, T. The implementation of technical energy efficiency and CO<sub>2</sub> emission reduction measures in shipping. *Ocean. Eng.* **2017**, *139*, 184–197. [\[CrossRef\]](#)
- Kuramochi, T.; Ramirez, A.; Turkenburg, W.; Faaij, A. Comparative assessment of CO<sub>2</sub> capture technologies for carbon-intensive industrial processes. *Prog. Energy Combust. Sci.* **2012**, *38*, 87–112. [\[CrossRef\]](#)
- Olajire, A.A. CO<sub>2</sub> capture and separation technologies for end-of-pipe applications—A review. *Energy* **2010**, *35*, 2610–2628. [\[CrossRef\]](#)
- Wilberforce, T.; Baroutaji, A.; Soudan, B.; Al-Alami, A.H.; Olabi, A.G. Outlook of carbon capture technology and challenges. *Sci. Total Environ.* **2019**, *657*, 56–72. [\[CrossRef\]](#)
- Wang, M.; Lawal, A.; Stephenson, P.; Sidders, J.; Ramshaw, C. Post-combustion CO<sub>2</sub> capture with chemical absorption: A state-of-the-art review. *Chem. Eng. Res. Des.* **2011**, *89*, 1609–1624. [\[CrossRef\]](#)
- Omogbe, O.; Mustapha, A.N.; Steinberger-Wilckens, R.; El-Kharouf, A.; Onyeaka, H. Carbon capture technologies for climate change mitigation: A bibliometric analysis of the scientific discourse during 1998–2018. *Energy Rep.* **2020**, *6*, 1200–1212. [\[CrossRef\]](#)
- Wall, T.F. Combustion processes for carbon capture. *Proc. Combust. Inst.* **2007**, *31*, 31–47. [\[CrossRef\]](#)
- Liu, Q.; Shi, Y.; Zhong, W.; Yu, A. Co-firing of coal and biomass in oxy-fuel fluidized bed for CO<sub>2</sub> capture: A review of recent advances. *Chin. J. Chem. Eng.* **2019**, *27*, 2261–2272. [\[CrossRef\]](#)
- Stanger, R.; Wall, T.; Spörl, R.; Paneru, M.; Grathwohl, S.; Weidmann, M.; Scheffknecht, G.; McDonald, D.; Myöhänen, K.; Ritvanen, J.; et al. Oxyfuel combustion for CO<sub>2</sub> capture in power plants. *Int. J. Greenh. Gas Control* **2015**, *40*, 55–125. [\[CrossRef\]](#)
- Wang, C.; Zhang, X.; Liu, Y.; Che, D. Pyrolysis and combustion characteristics of coals in oxyfuel combustion. *Appl. Energy* **2012**, *97*, 264–273. [\[CrossRef\]](#)
- Shen, Q.; Zheng, Y.; Luo, C.; Zheng, C. Development and characterization of Ba<sub>1-x</sub>Sr<sub>x</sub>Co<sub>0.8</sub>Fe<sub>0.2</sub>O<sub>3-δ</sub> perovskite for oxygen production in oxyfuel combustion system. *Chem. Eng. J.* **2014**, *255*, 462–470. [\[CrossRef\]](#)
- Shen, Q.W.; Zheng, Y.; Luo, C.; Zheng, C.G. Characteristics of SrCo<sub>1-x</sub>Fe<sub>x</sub>O<sub>3-δ</sub> perovskite powders with improved O<sub>2</sub>/CO<sub>2</sub> production performance for oxyfuel combustion. *Bull. Korean Chem. Soc.* **2014**, *35*, 1613–1618. [\[CrossRef\]](#)
- Eyring, V.; Isaksen, I.S.; Berntsen, T.; Collins, W.J.; Corbett, J.J.; Endresen, O.; Grainger, R.; Moldanova, J.; Schlager, H.; Stevenson, D.S. Transport impacts on atmosphere and climate: Shipping. *Atmos. Environ.* **2010**, *44*, 4735–4771. [\[CrossRef\]](#)
- Carrasco-Maldonado, F.; Spörl, R.; Fleiger, K.; Hoening, V.; Maier, J.; Scheffknecht, G. Oxy-fuel combustion technology for cement production—State of the art research and technology development. *Int. J. Greenh. Gas Control* **2016**, *45*, 189–199. [\[CrossRef\]](#)
- Görke, R.; Marek, E.; Donat, F.; Scott, S. Reduction and oxidation behavior of strontium perovskites for chemical looping air separation. *Int. J. Greenh. Gas Control* **2020**, *94*, 102891. [\[CrossRef\]](#)
- Zhang, T.; Li, Z.; Cai, N. Continuous O<sub>2</sub>-CO<sub>2</sub> production using a Co-based oxygen carrier in two parallel fixed-bed reactors. *Korean J. Chem. Eng.* **2009**, *26*, 845–849. [\[CrossRef\]](#)

22. Perez, P.L.; Boehman, A.L. Experimental study of oxygen-enriched diesel combustion using simulated exhaust gas recirculation. *J. Eng. Gas Turbines Power* **2009**, *131*, 1–11. [[CrossRef](#)]
23. Shen, Q.; Zheng, Y.; Luo, C.; Ding, N.; Zheng, C.G.; Thern, M. Effect of A/B-site substitution on oxygen production performance of strontium cobalt based perovskites for CO<sub>2</sub> capture application. *RSC Adv.* **2015**, *5*, 39785–39790. [[CrossRef](#)]
24. Ding, H.R.; Xu, Y.Q.; Luo, C.; Zheng, Y.; Shen, Q.W.; Liu, Z.H.; Zhang, L.Q. Synthesis and characteristics of BaSrCoFe-based perovskite as a functional material for chemical looping gasification of coal. *Int. J. Hydrogen Energy* **2016**, *41*, 22846–22855. [[CrossRef](#)]
25. Jiang, Y.H.; Shen, Q.; Li, S.; Yang, G.; Huang, N.B. B-site cobalt-doped perovskite oxide BaNiO<sub>3</sub> oxygen sorbents for performance improvement of oxygen enriched gas production. *New J. Chem.* **2020**, *44*, 6003–6009. [[CrossRef](#)]
26. Ding, H.R.; Xu, Y.Q.; Luo, C.; Wang, Q.Y.; Shen, C.; Xu, J.X.; Zhang, L.Q. A novel composite perovskite-based material for chemical-looping steam methane reforming to hydrogen and syngas. *Energy Convers. Manag.* **2018**, *171*, 12–19. [[CrossRef](#)]
27. Wang, Q.Y.; Luo, C.; Li, X.S.; Ding, H.R.; Shen, C.; Cao, D.S.; Zhang, L.Q. Development of LaFeO<sub>3</sub> modified with potassium as catalyst for coal char CO<sub>2</sub> gasification. *J. CO<sub>2</sub> Util.* **2019**, *32*, 163–169. [[CrossRef](#)]
28. Ding, H.R.; Luo, C.; Li, X.S.; Cao, D.S.; Shen, Q.W.; Zhang, L.Q. Development of BaSrCo-based perovskite for chemical-looping steam methane reforming: A study on synergistic effects of A-site elements and CeO<sub>2</sub> support. *Fuel* **2019**, *253*, 311–319. [[CrossRef](#)]
29. Yi, J.X.; Weirich, T.E.; Schroeder, M. CO<sub>2</sub> corrosion and recovery of perovskite-type BaCo<sub>1-x-y</sub>Fe<sub>x</sub>Nb<sub>y</sub>O<sub>3-δ</sub> membranes. *J. Memb. Sci.* **2013**, *437*, 49–56. [[CrossRef](#)]
30. Shen, Q.W.; Zheng, Y.; Li, S.A.; Ding, H.R.; Xu, Y.Q.; Zheng, C.G.; Thern, M. Optimize process parameters of microwave-assisted EDTA method using orthogonal experiment for novel BaCoO<sub>3-δ</sub> perovskite. *J. Alloy. Compd.* **2016**, *658*, 125–131. [[CrossRef](#)]
31. Singh, D.V.; Pedersen, E. A review of waste heat recovery technologies for maritime applications. *Energy Convers. Manag.* **2016**, *111*, 315–328. [[CrossRef](#)]